ASTRONOMY & ASTROPHYSICS
SUPPLEMENT SERIES

Astron. Astrophys. Suppl. Ser. **108,** 513-532 (1994)

Deep Hα survey of the Milky Way. II. The $l = 328°$ area*

Y.M. Georgelin[1], P. Amram[1], Y.P. Georgelin[1], E. le Coarer[1,2] and M. Marcelin[1]

[1] Observatoire de Marseille, 2 Place Le Verrier, F-13248 Marseille Cedex 04, France
[2] Observatoire de Grenoble, BP. 53X, Grenoble Cedex, France

Received April 7; accepted June 23, 1994

Abstract. — The detailed velocity field of the ionized hydrogen over an area of about 4° × 3° around galactic longitude 328° has been obtained in the frame of an Hα Survey of the galactic plane carried out at ESO La Silla. The detailed analysis of the Hα profiles shows that there are several layers of ionized hydrogen with different velocities. Besides individual HII regions there are two diffuse nebular emissions detected all over the studied area with velocities −20 km s^{-1} and −40 km s^{-1}. The HII regions exhibit complex structures; according to their velocities they can be divided into two groups around −40 km s^{-1} and −47 km s^{-1}. We have studied in detail the structure and velocities of the bright HII regions. The well known narrow lines of RCW94 are confirmed. The distances of the O-B3 stars in this area have been calculated from the literature data, and combined with radio data and our Hα data allow us to determine the distances of the nebular components. We find that the faint ionized gas layer at −20 km s^{-1}, never detected before, neither at optical nor at radio wavelengths, is at about 1 kpc and defines the Sagittarius Carina arm at longitude 328°. This implies that the main HII regions in this area and the diffuse ionized hydrogen in which they are immersed belong to a second arm (probably the Scutum Crux arm). This arm appears split at this longitude with two groups at 2.3 and 3 kpc. The radiosource 327.759 − 0.351 at H109α V_{LSR} = −72 km s^{-1} (d_{kin} = 4.5 kpc) has been detected at Hα wavelength behind the other Hα emissions.

Key words: interstellar medium: HII regions — Galaxy: structure

1. Introduction

The interferometric observations of HII regions at Hα wavelength that we are carrying out with a small telescope at La Silla (Amram et al. 1991; le Coarer et al. 1992: Paper I), should allow us to specify the structure of the spiral arms of our Galaxy. Therefore we have chosen to cover various areas of the galactic plane selected as a function of their richness in HII regions (Hα or H109α) and of their strategic position for determining the number and location of the different spiral arms in the 4th galactic quadrant (Marcelin et al. 1993).

The region studied here is lying in the constellation Norma between $l = 326°$ and $l = 330°$ and b between 1° and −2° ($15^h36^m < \alpha < 16^h04^m$ and $-55°30' < \delta < -52°50'$). The line of sight crosses several spiral arms at these galactic longitudes. The ESO Sky Survey plates clearly show that this area is located between a star-rich area (to the east and to the south) and a comparatively depleted area (to the north and to the west). As a consequence, we expect that the interstellar extinction is strongly variable over the observed area.

Several HII regions have been identified by Rodgers et al. (1960) in this area, RCW94 and RCW95 at $l = 326°5$, $b = 0°8$ and RCW96 to RCW99 near $l = 328°$, $b = -0°8$. Concerning OB stars a small association named Norma OB1 ($l = 328°$, $b = -1°$) by Lynga (1964) was studied by Bok et al. (1963 and 1967) and Drilling (1972). All of them concluded that there is a single group at a distance of 2.3 to 2.5 kpc. At higher longitudes however, in the group of OB stars at $l = 332°$, $b = -1°$ also noted by Lynga (1964), Westerlund (1969) found evidence for 2 distinct groups of OB stars at 3.9 kpc and 1.8 kpc seen in projection. Similarly Hα observations show two distinct velocity groups corresponding to two values of distances for the HII regions at this longitude (Georgelin & Georgelin 1970a). A review of the material on optical and radio spiral tracers in the Norma area available at that time was made by Rydgren (1974).

Since then the radial velocities of the ionized hydrogen of the HII regions around $l = 326°$, 328° and 332° (see deep Hα photographs of these regions in Georgelin & Georgelin 1970b) have been measured with fixed-order in-

*Based on observations collected at the European Southern Observatory

terferograms and analysed in relation with H109α data (Georgelin & Georgelin 1976). It has been shown that, at $l = 326°$, the H109α source 326.5 + 0.9 is related to RCW94 and that 326.6 + 0.6 coincides with an uncatalogued nebula near RCW95. The radial velocities of all these regions at $l = 326°$ are in agreement around -40 km s^{-1}, and they form a single complex. At $l = 328°$ the radial velocities of the different emission sources remain between -40 km s^{-1} and -50 km s^{-1} and no HII region with less negative velocity was found. In contrast to this, at $l = 332°$ besides numerous distant H109α sources, there are clearly two groups of HII regions with velocities near -50 km s^{-1} and near -20 km s^{-1} that were attributed respectively to spiral arms Sagittarius-Carina and Scutum-Crux (as named by Georgelin & Georgelin 1976).

Since no foreground HII regions were found at $l = 328°$ and since OB stars were found at a distance falling between these two spiral arms it was impossible to conclude about the membership to an arm for any of the HII regions seen at that longitude. Furthermore the range in radial velocities seems a bit too large for a single complex of HII regions. Even more puzzling is the difference between the Hα and radio continuum appearance as seen in Fig. 1. To clarify the problem we decided to reexamine this area in the light of the data of our new Hα Survey.

The observations are described in Sect. 2 with some emphasis on the data reduction. Section 3 gives the results of the present Hα observations. Section 4 is devoted to the study of OB stars from the literature in the same area. In Sect. 5 we discuss these results together with radio data in terms of galactic structure.

2. Observations and data reduction

The observations have been made in the frame of an Hα Survey of the Milky Way carried out at ESO La Silla with a 36-cm diameter telescope. It is equipped with a focal reducer, a scanning Fabry-Perot interferometer and a 2D photon counting system. A complete description, including data acquisition and reduction techniques, has been given in Amram et al. (1991) and Paper I.

Let us recall that data cubes (x,y,λ) are obtained in a 38' × 38' field with a spatial resolution of 9" × 9". Two different Fabry-Perot interferometers are available on the telescope, one with interference order $p = 796$ offering a spectral sampling of 16 km s^{-1} with 24 scanning steps and another one (used since 1991) with interference order $p = 2604$ offering a sampling of 5 km s^{-1}. More than half of the fields studied here were observed with the higher spectral resolution (see Table 1). The wavelength calibration is obtained by scanning the emission line of a hydrogen lamp before and after each observation (to check stability of the interferometer). The instrumental profile is deduced from calibration scans of a narrow line of a Neon lamp at 6598.95 Å. Two interference filters were used for these observations. The first one, centered at 6563 Å with a FWHM of 11 Å, was quite old and suffered bandwidth shifts (up to 8 Å) from the center to the edge of the Hα field of view, making it difficult to subtract the OH parasitic night sky lines (for instance the lines at 6553.6 Å and 6568.8 Å being at the edges of the bandpass appeared to change in intensity across the field). The second one, used with the high-resolution interferometer, is centered at 6562 Å and has a FWHM of 11 Å; its bandwidth is stable over the whole field. For each filter and for each observing run the observations were flat-fielded using a sum of interferograms obtained with a continuum lamp observed through the same filter and interferometer set.

Table 1. Observations

Obs.	α 1950 h m s	δ* ° '	date**	exp. time (s)	Int. (p)	geo.Hα (ev/px/h)
023	15 49.5	-54 05	4/26/90	4560	796	0.8
026	NS		4/27/90	3120	796	0.4
027	15 51.0	-53 35	4/27/90	9600	796	0.5
028	15 54.9	-53 34	4/27/90 e	3160	796	1.1
036	15 44.9	-54 14	4/29/90	13320	796	0.7
039	15 42.2	-53 55	4/30/90	7920	796	0.6
043	15 44.9	-54 18	5/01/90	9960	796	0.4
044	NS		5/01/90 e	6480	796	1.3
046	15 38.5	-54 03	5/02/90	5520	796	0.3
047	15 53.3	-54 13	5/02/90	5760	796	0.7
048	15 47.1	-54 41	5/03/90	4176	796	0.6
049	15 50.1	-54 45	5/03/90 e	4128	796	1.4
083	15 53.4	-54 17	4/16/91 e	5520	2604	0.8
086	15 50.6	-53 54	4/17/91	7200	2604	0.3
087	15 49.0	-53 16	4/17/91	2040	2604	0.7
090	15 40.0	-53 16	4/18/91	6969	2604	0.4
091	15 49.4	-55 12	4/18/91 e	5880	2604	0.6
094	15 57.9	-54 09	4/19/91	7200	2604	0.3
095	NS		4/19/91 e	7440	2604	0.5
098	16 01.7	-54 25	4/20/91	7320	2604	0.2
099	15 53.4	-53 04	4/20/91 e	7320	2604	0.5
269	15 49.6	-54 32	2/19/93 e	4800	2604	0.8
278	15 55.1	-54 09	2/22/93 e	8040	2604	0.8
284	15 45.9	-54 05	2/24/93 e	7200	2604	0.8
287	15 53.4	-53 41	2/25/93 e	7200	2604	0.8
290	16 01.5	-54 57	2/26/93 e	7800	2604	0.7
293	15 57.3	-53 21	2/27/93 e	7200	2604	0.8

*NS (for night sky) means that the observation was made far from the galactic plane for monitoring the night sky lines.
**e means that the observation was made at the end of the night.

Table 1 lists the observations used for this paper. One can see that they have been obtained at three different epochs. The last two sets of observations were made with the new combination of filter and interferometer (Fabry-Perot $p = 2604$). Observations indicated with "NS" (for night sky) were made far from the galactic plane in order to check the relative intensity of the night sky lines (known to be highly variable with the epoch of observation). Since

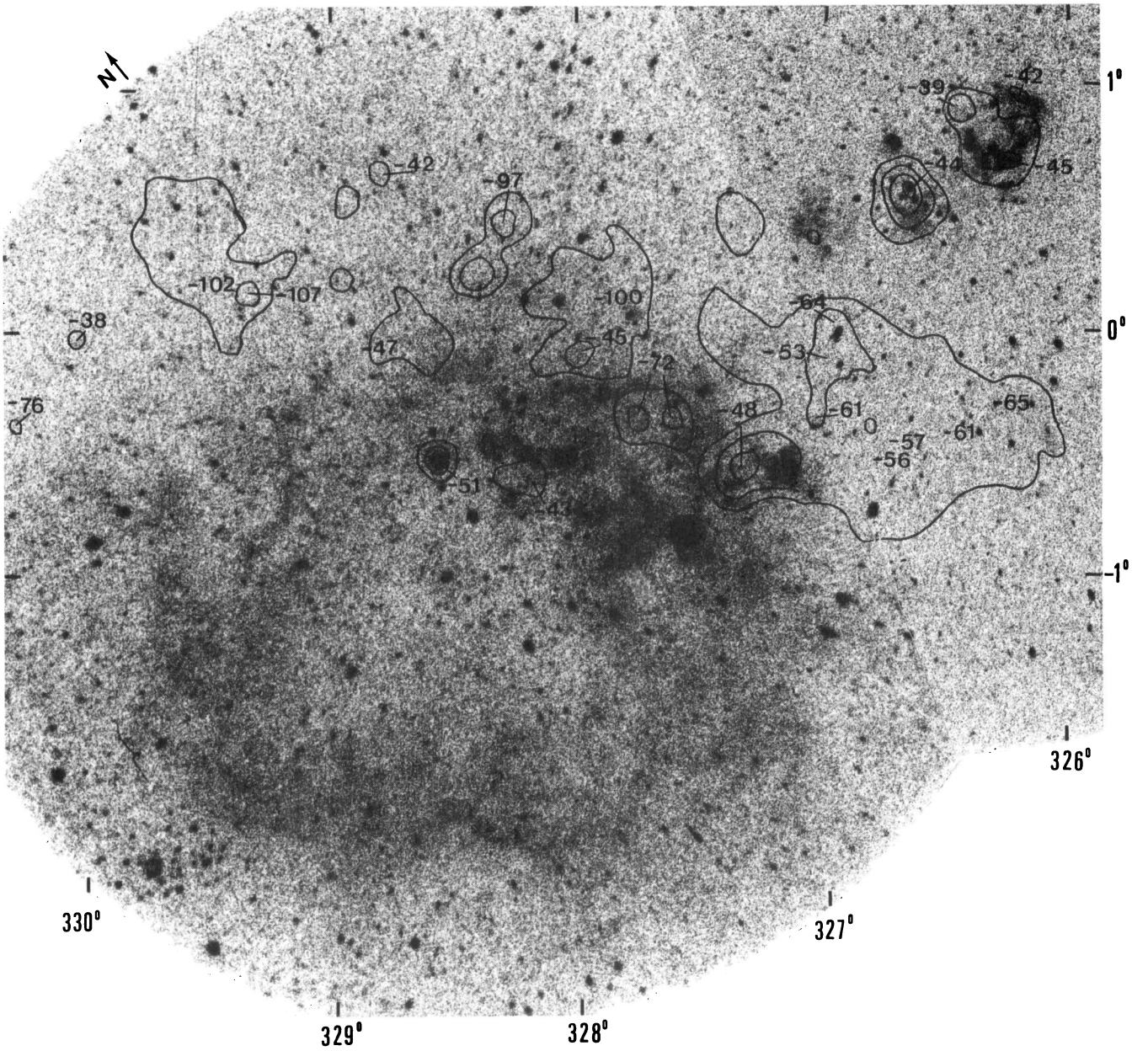

Fig. 1. Hα photograph of the studied area (Georgelin & Georgelin 1970b). The isophotes 1, 2, 4 and 8 Jy of the 5 GHz continuum charts of Haynes et al. (1978) have been superposed. The radial velocities of H109α and H110α hydrogen recombination line (Caswell & Haynes 1987), observed with a beamsize of 4'4 at the positions of continuum intensity peaks, are indicated

the transparency of the sky may change considerably from one observation to the next the exposure times given in Table 1 are not directly connected with the expected Signal to Noise ratio. On the contrary long exposures were often made to compensate for poor transparency conditions. The last column indicates the intensity of the maximum of the geocoronal Hα night sky line (in events/pixel/hour for easier comparison) measured for each observation in areas as free of nebular emission as possible. One can see that this emission is systematically brighter for observations made at the end of the night (identified by letter e written after the date). This effect was not observed for OH night sky lines. Apart from this variation, the intensity of the Hα geocoronal emission line remained fairly constant for a given observing run (compare for instance the values found at the end of the night for each run).

For the first series of observations (S023 to S049) made with the Fabry-Perot interferometer of low interference order (p = 796) and the interference filter which suffered from bandwidth problems, the parasitic OH lines 6553.6

and 6568.8 (generally lower than 1 event/px/hour) were difficult to subtract. Their relative intensities in each location of the field were determined by using the observations made far from the galactic plane. However velocities of faint nebular emission (around 1 event/px/hour) are badly determined. For the last series of observations (S083 to S293) the interference filter had no transmission problem and the Fabry-Perot interferometer of higher interference order ($p = 2604$) has been chosen in order to have the two OH lines (which belong to different interference orders) superposed on the same spectral channel. These OH lines are less than 0.3 event/pixel/hour.

Calibrating the fluxes may be done only indirectly, generally with HII regions for which absolute photometry exists. See for instance le Coarer et al. (1993) for SMC observations made with the same instrument. One can say then that a gaussian line with a peak height of 1 event/px/hour and a FWHM of 25 km s^{-1} corresponds to an HII region with emission measure about 20 cm^{-6}, pc. Of course this is only a very rough estimate since several causes of uncertainty may add together.

Besides the problem of night sky lines subtraction, the analysis of our data is complicated because several velocity components are encountered in this area, overlapping everywhere in the field. Indeed except towards a few bright HII regions (those listed by Rodgers et al. 1960) for which the Hα profile may be fitted by a single velocity component, most of the profiles exhibit complex shapes. Our data, once flat-fielded and corrected for dark current, were analysed methodically as follows:

- A detailed mapping of the instrumental profile in each selected area is done using the narrow-profile line Ne 6598.95 Å from a Neon lamp. With the Fabry-Perot interferometer $p = 2604$ the profile width is found to be 13 km s^{-1} at the center and increases toward the edges where it is almost twice the central value (Paper I).
- The night skylines are well fitted by the instrumental profile, and they are subtracted according to this fit.
- The nebular lines are clearly wider and must be fitted by the convolution of the instrumental profile with a gaussian, the width of which depends on the nebular properties (typically this width is around 25 km s^{-1}). Inside each selected area we look for the set of nebular lines the sum of which fits the observed Hα profile best. Because of the intrinsic width of the different nebular components superimposed along one line of sight and due to their small velocity differences several solutions are often possible for a given profile, with different sets of nebular components giving the same total Hα profile. However the analysis of the variations of this profile across each 38' × 38' field and then across the mosaic covering the whole selected area enables one to distinguish unambiguously the nebular components actually observed.

The best way to identify the main nebular components for a given field is to look at the λ maps (the optical equivalent of channel maps, i.e. maps where the Hα emission is displayed through narrow velocity steps). Figure 2 shows an example of these λ maps for two contiguous fields in the central part of the mosaic of fields covering the $l = 328°$ area (Fig. 3). The 3 maps selected for Fig. 2 are centered at velocities $V_{LSR} = -17$ km s^{-1}, -36 km s^{-1}, -50 km s^{-1}, each one covering 5 km s^{-1}. These maps are approximately centered on the main components identified in this area. Such maps allow one to select the areas having one of the components clearly predominant which makes the decomposition of the total profile easier. The intensity of each component is highly variable across the field and most of the time the faintness of the signal forces one to add the Hα profiles of several contiguous pixels in order to obtain a sufficient signal to noise ratio, necessary for an accurate study of the behaviour of each component across the field.

3. Results

The kinematical results are represented in Fig. 3 which shows the mosaic of 24 fields observed in the selected area at galactic longitude $l = 328°$. Each elementary image is the simple addition of the series of interference patterns obtained inside one 38' × 38' field, flat-fielded and corrected for image distortion. It is more or less equivalent to the image that would be obtained directly through an interference filter with a bandwidth of 2.4 Å. This is why stars remain visible whereas they are less visible on λ maps (see Fig. 2 for instance) for which emission is obtained in a narrower band. Because of differences in exposure times and transparency conditions the intensities inside each elementary field had to be adjusted by eye from place to place for a better display.

In Fig. 3b, drawn on the same scale as Fig. 3a, we show in a schematic manner the main velocity components detected over this area. Different types of lines delineate the contours of the different nebular components. It must be noted that there is no region completely free from nebular emission. The velocities found for these diffuse components are indicated between parentheses on the map.

3.1. *Diffuse emission at −20 km* s^{-1}

The first diffuse component is found at $V_{LSR} = -20$ km s^{-1} with a minimum of 0.1 event/pixel/h at the top of the emission line but generally much brighter. In Fig. 3b we delineated the enhancements of this component (peak line higher than 0.5 event/pixel/h) with a dashed line. The presence of such enhancements is a guarantee that the faint diffuse emission detected at -20 km s^{-1} over the whole of the observed area is real. Three of the nebulae are particularly interesting, and we named them according to their galactic coordinates Hα 327.8 − 0.9, Hα 327.0 − 1.2 and Hα 328.2 − 2.0 (see notes to Table 4 for the corresponding α δ coordinates). Hα 327.8 −

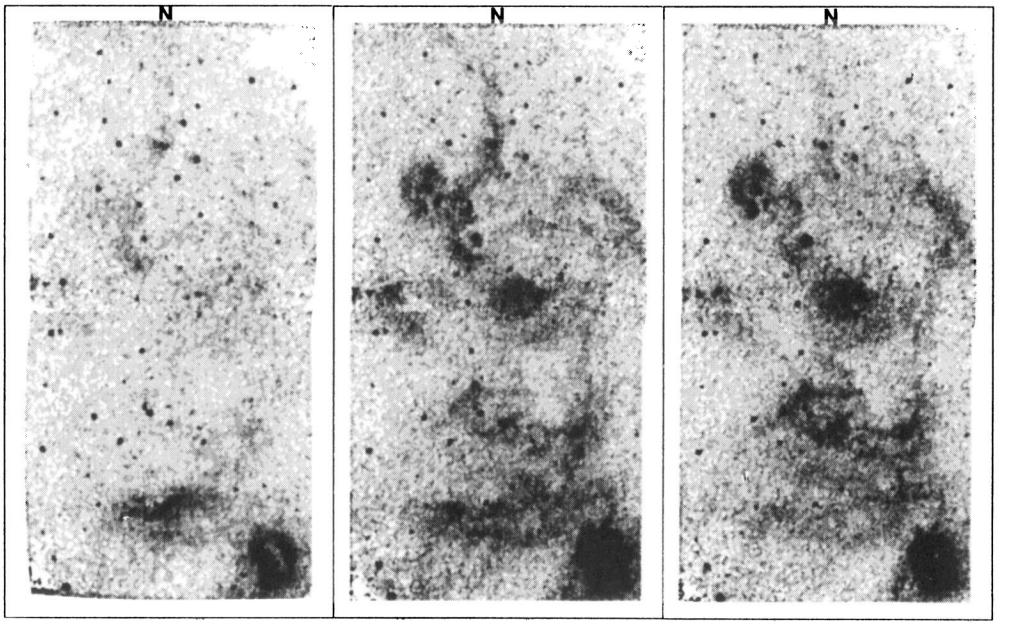

Fig. 2. Examples of 3 λ maps (Hα emission through velocity steps of 5 km/s) for a mosaic of two adjacent fields situated at the center of Fig. 3. The central velocities of these maps are $V_{LSR} = -17$, -36 and -50 km/s from left to right. HII regions with different radial velocities are thus clearly separated

0.9 exhibits an Hα profile dominated by a component at $V_{LSR} = -19$ km s^{-1}, reaching 8 events/px/h at its maximum. This bright nebula was already clearly visible in the raw data while observing (see Fig. 4 of Amram et al. (1991) where it shows up in deep blue on the velocity map). Hα 327.0 − 1.2 is found at $V_{LSR} = -23$ km s^{-1} and reaches 1 event/px/h at maximum height. The third one (328.2 − 2.0) is fainter. We shall see later that these three nebulae are excited by stars at distances of around 1 kpc.

3.2. *Diffuse emission at −40 km s^{-1}*

This component is also detected all over the mosaic, even in "empty" fields. Its minimum intensity is generally equal to or slightly higher than that of the −20 km s^{-1} component and its velocity generally lies between −40 km s^{-1} and −45 km s^{-1}. However in the southeastern part of the mosaic (around 16^h03^m, −55°05') and in the southern part (around 15^h49^m, −55°20') it may reach −50 km s^{-1}.

Two supplementary marginal components are suspected. They are much fainter, less than 0.1 event/pixel/hour. The first one is found almost all over the mosaic with velocities between 0 km s^{-1} and −5 km s^{-1}, and is (very) local emission. The second one, around −60 km s^{-1}, is found between 15^h44^m and 15^h49^m and −54°and −55°. This highly negative velocity suggests a large distance, implying in turn a large dimension for the corresponding HII region. Such extended sources have been detected in this direction in radio continuum as well, as discussed in Sect. 5. Unfortunately this negative component is detected in fields observed in 1990, with the lower resolution, and its reality is doubtful.

3.3. *Discrete HII regions at −40 km s^{-1} and −50 km s^{-1}*

The HII regions one can see on the mosaic of Fig. 3a form a patchy structure, with filaments and absorption patterns. The velocity field too is quite complicated. Most of the HII regions seen in this area have velocities ranging from −37 km s^{-1} to −50 km s^{-1}. Two main velocity groups may be distinguished, sometimes coinciding along the line of sight. The first group, with velocities between −37 km s^{-1} and −42 km s^{-1}, is schematically drawn in Fig. 3b with continuous contours. We will call it the −40 km s^{-1} group. The second group, with more negative velocities (between −43 km s^{-1} and −50 km s^{-1}) has its contours marked out with a dotted line. One can see that the two groups are intricately overlapped but that any given filament or patch of nebula keeps the same velocity all along its extension.

The velocities of bright HII regions also exhibit two distinct groups: RCW94, 95 and 98 with velocities around −40 km s^{-1} and RCW96, 97 and 99 around −50 km s^{-1}. We shall now study them in detail.

3.3.1. RCW94-95 complex, at $l = 326°$ and $V_{LSR} = -40$ km s^{-1}

Figure 4a shows the HII regions of this complex. An image such as this is obtained by adding the λ maps containing Hα emission from these regions (see last paragraph of

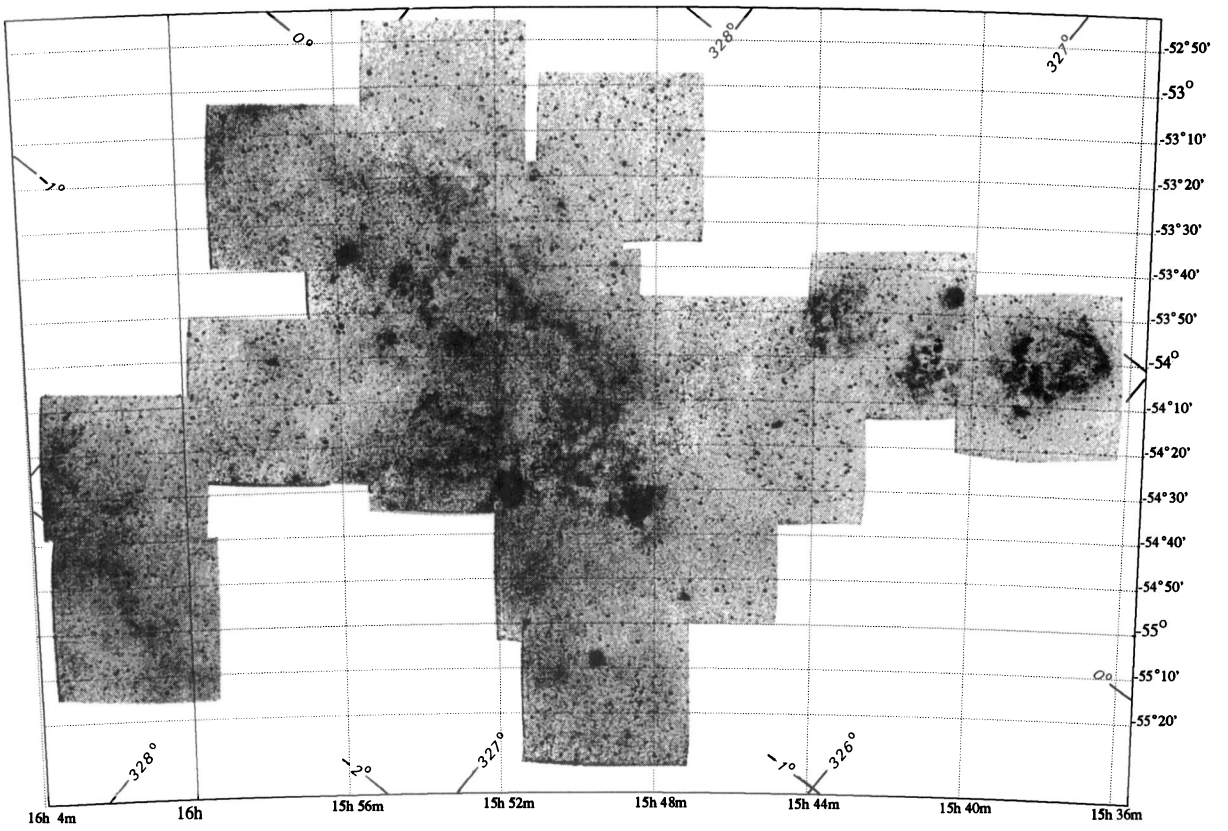

Fig. 3. a) Mosaic of the observed fields in the 328° area. Each image is obtained by adding all λ maps over the free spectral range, then flat-fielded and corrected for the distortion. It is equivalent to a photograph obtained through a filter with a 2.4 Å bandwidth

Sect. 2 for definition of λ maps). It is a pure monochromatic image with a bandwidth of 0.3 Å. Comparing Fig. 4a with previously published photographs of this region (e.g. Plate 1 of Shaver et al. 1983) one can see that the nebulae are much more fluffy and patchy, with a lot of condensations. Furthermore the different HII regions seem to be connected through dust lanes and faint emission structures. A careful examination of the Hα profiles in seemingly empty areas (adding them up when necessary to increase the S/N ratio) shows that a faint diffuse emission at the same velocity as the HII regions is also detected all over the field (see Sect. 3.2). We note that another component, still fainter, is detected with a velocity ranging between -15 km s^{-1} and -20 km s^{-1} (Sect. 3.1).

3.3.2. RCW94

This HII region is well known for its narrow emission lines (Shaver et al. 1979 and 1983). Shaver et al. (1983) have observed radio recombination lines in RCW94 with a half power beamwidth of 4.5 × 4.5 arcmin. Table 2 gives the velocity and line width they measured, together with Caswell and Haynes (1987) values for sources at $l = 326°$. For a good comparison of our results with these radio results we added our Hα profiles in pixels approximately covering the radio beam. Our Hα velocities and line widths (deconvolved from the instrumental response) are given in the last two columns of Table 2. One can see the perfect agreement between radio H109α and optical Hα, for velocities as well as line widths. The only significant discrepancy is the line width of region 326.441 + 0.914, quite large at H109α while being equal to values found for RCW94 in Hα. The Hα emission measured there is thus probably an extension of RCW94 and not the radiosource itself although they appear to be linked in radio continuum emission.

Contrary to radio observations, integrated over a large beam at discrete locations, our Hα observations enable a detailed and continuous study of the ionized gas. Figure 4b schematically shows the velocities and linewidths measured in each condensation of the field of Fig. 4a. The velocities and linewidths remain practically constant inside a given HII region. Only RCW94 exhibits narrow linewidths; the linewidths are fairly normal (although still rather narrow) for the other HII regions. The most disturbed nebula is that connected with 326.645 + 0.589, with velocities ranging from -34 km s^{-1} to -44 km s^{-1} and linewidths ranging from 19 km s^{-1} to 36 km s^{-1}.

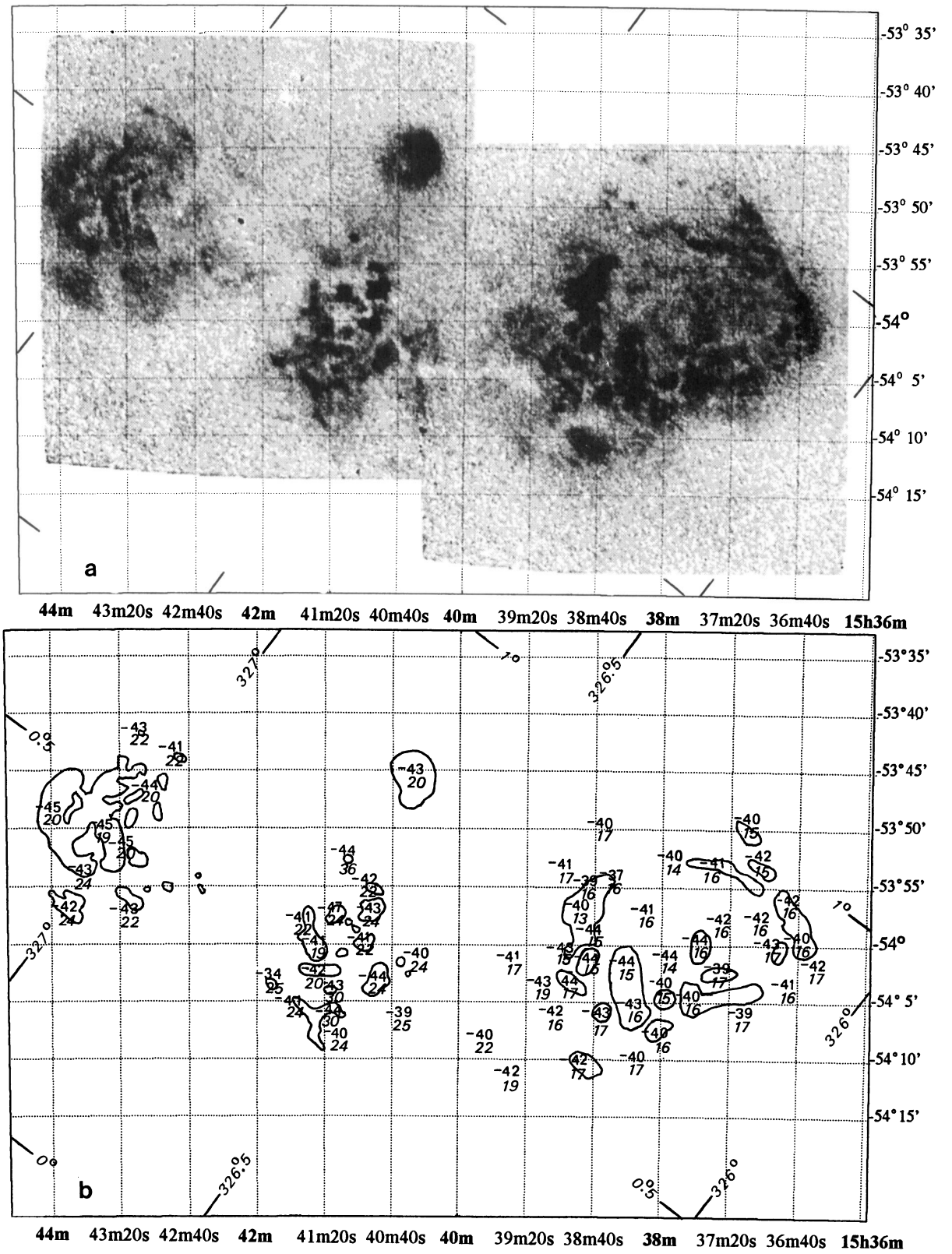

Fig. 4. a) Monochromatic image of the HII region group RCW94-95 at $l = 326°$ obtained by adding the λ maps corresponding to the Hα line. b) Radial velocities with line width (FWHM), in italics under it, deconvolved from the instrumental line for each condensation

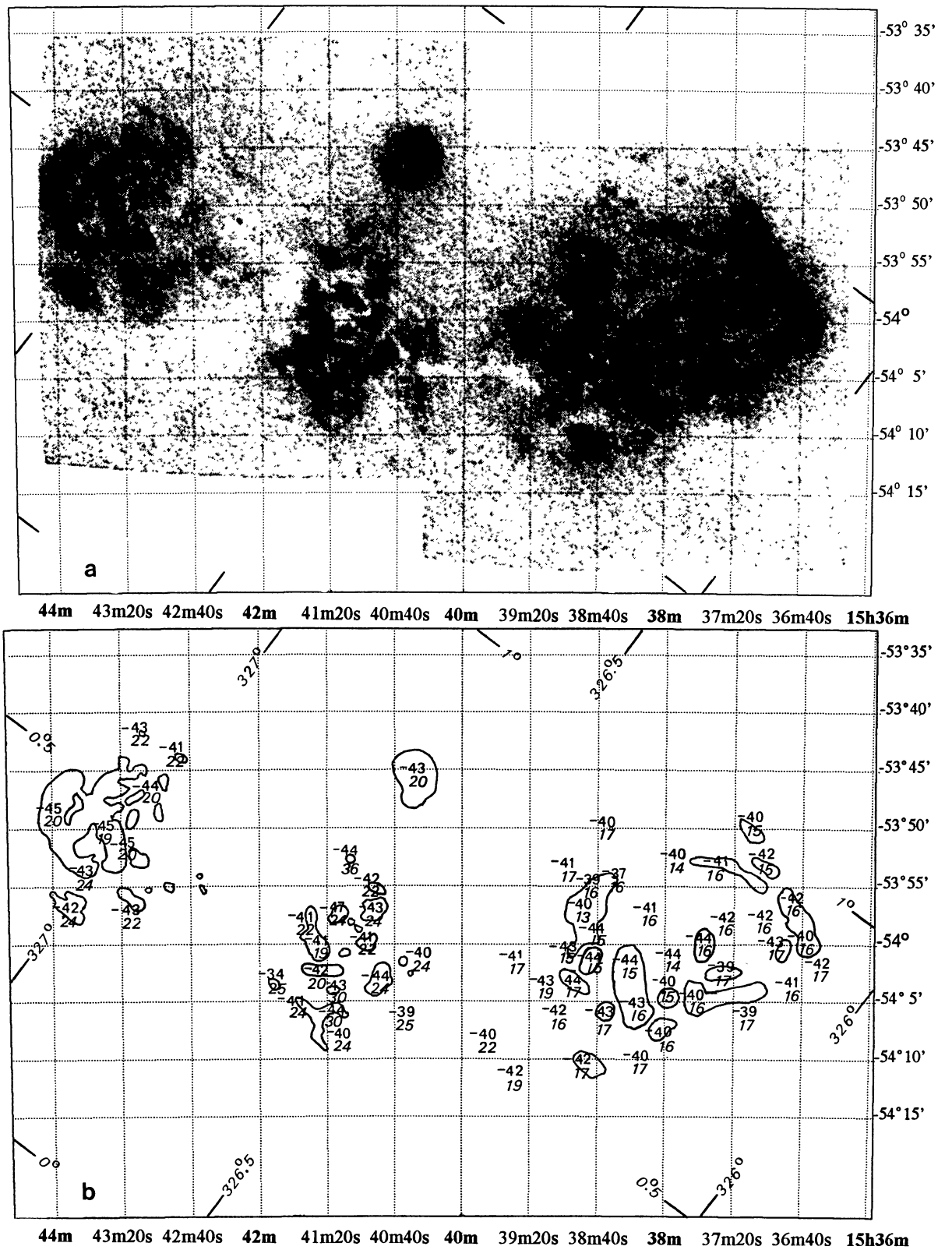

Fig. 4. a) Monochromatic image of the HII region group RCW94-95 at $l = 326°$ obtained by adding the λ maps corresponding to the Hα line. b) Radial velocities with line width (FWHM), in italics under it, deconvolved from the instrumental line for each condensation

Table 2. Velocities and line widths of the HII regions at $l = 326°$

Source	α	δ	H109α			Hα	
	h m s	° ' "	V km/s	ΔV km/s	R	V km/s	ΔV km/s
RCW94.1	15 38 13	-54 06 45	-43.1	14.9	1	-43	16
RCW94.2	15 38 45	-53 56 27	-39.6	13.2	1	-40	16
			-51.9	18.1	1		
RCW94.3	15 38 23	-54 02 00	-45.1	15.6	1	-44	15
RCW94.4	15 36 48	-53 55 45	-39.9	16.0	1	-42	16
326.230+0.976	15 37 01	-53 53 23	-42	14	2	-42	15
326.315+0.689	15 38 38	-54 04 10	-45	15	2	-44	15
326.441+0.914	15 38 25	-53 48 50	-39.0	26.8	1	-40	17
			-39	27	2		
326.645+0.589	15 40 50	-53 57 03	-44.1	27.3	1	-43	25
			-44	27	2		

References: (1) *Shaver et al.* (1983), (2) *Caswell & Haynes* (1987)

3.4. *Hα emission at −65 km s^{-1}*

In Fig. 3b one can see a small region at $15^h50\overset{m}{.}7$, −54°0' with a strongly negative velocity, around −65 km s^{-1}. The Hα profiles observed there clearly show a bump toward the short wavelengths which is not seen at all positions surrounding this region. This is the signature of additional Hα emission with an intensity around 0.5 event/pixel/hour, slightly brighter than the diffuse emission at −20 km s^{-1} detected all over the observed area. We shall see in Sect. 4 that radio sources with velocity −72 km s^{-1} have been found in this direction, strongly suggesting that we indeed detected such distant radio sources in Hα. Because of the faintness of this Hα emission the measure of its radial velocity is not accurate enough and we will use the H109α velocity value to determine the kinematic distance (Sect. 5.2.3). Velocities of around −60 km s^{-1} have also been found in the easternmost part of the mosaic (see Fig. 3b). However the detection of such a negative velocity component outside the galactic plane ($b = -2°$ in this case) raises a serious problem. Even at the near distance of about 4 kpc this corresponds to $z = -140$ pc, clearly more than the ionized hydrogen scale height at this position in the Galaxy. Extending the observations to adjacent fields toward the east should help in clarifying this point.

4. OB Stars

The Hα velocities discussed in Sect. 3 may be interpreted meaningfully only when they are combined with stellar distances, especially of exciting stars. There are few individual HII regions with identified exciting stars in the observed area. Since ionized hydrogen is detected all over the studied area we searched the literature for all stars of spectral type O to B3 in this region ($\alpha_{1950} = 15^h36^m$ to 16^h04^m, $\delta_{1950} = -53°$to $-55°30'$). Averaging the photometric data (U,B,V,$H\beta$) spectral type and radial velocities found in the literature (using the Strasbourg CDS data base) we computed the distances to each star. The results are given in Table 3. We used the absolute magnitude-spectral type calibration of Humpreys & Mac Elroy (1984) together with the intrinsic color index-spectral type calibration of Schmidt Kaler (1983). For the spectral types and luminosity classes considered here the use of different absolute magnitude calibrations currently available in the literature could bring differences around 0.2 magnitudes for main sequence stars and up to 0.5 magnitudes for supergiants. The β indices were adjusted to absolute magnitudes of Humphreys & Mac Elroy. When neither spectral type nor Hβ are available, the results (given between parenthesis in Table 3) are based on UBV photometry alone, assuming that the stars belong to luminosity class V and using the relation:
$E(U-B)/E(B-V) = 0.72 + 0.05\ E(B-V)$.
The relation between total visual absorption A_V and the $(B-V)$ color excess is taken as 3.1.

The accuracy of derived distances remains poor, even when a spectral type or a β index is known. For instance in the case of LSS 3423, which is probably the main exciting star of RCW98, one finds a distance of 2.2 kpc from the β index while the 09IV spectral type indicates a distance of 3.5 kpc. The uncertainty on distances mainly comes from the uncertainty on the absolute magnitude resulting from difficulties in the spectral classification. Comparing different spectral classifications available for some stars of Table 3 one finds average differences of one spectral class and one luminosity class. A one luminosity class error may raise a difference of one magnitude in absolute magnitude thus changing for instance a distance of 2.5 kpc to 4 kpc. In Table 3 the following information is given:
Column 1: Star number in the Luminous Southern Star Catalogue (Stephenson & Sanduleak, 1971).
Column 2: Identification in one of the following catalogues classified in priority order: HD or CPD or BDMW (Bassino et al. 1982) or MF (Muzzio & Forte 1975) or D (Drilling 1972).
Column 3: Spectral type. The main sources are Garrison et al. (1977), Bassino et al. (1982), Humphreys (1975).

Column 4: Spectral type roughly estimated from *UBV* and Hβ photometry.
Columns 5, 6, 7: V, $B-V$, $U-B$. We give average values from the CDS data base, mainly Schild et al. (1983), Klare & Neckel (1977), Drilling (1972 and 1991), Muzzio & Forte (1975), Bassino et al. (1982).
Column 8: β index. The value is an average of values found in the CDS data base. The main sources are Klare & Neckel (1977), Drilling (1972), Muzzio & Forte (1975). β indices of emission line stars are not reported here.
Column 9: Heliocentric radial velocity ($V_{\rm hel}$) of the star from the CDS data base, complemented by data from Bassino (1985) and Drilling & Perry (1981).
Column 10: Adopted absolute magnitude, M_V. When both MK type and β index are available the adopted value is the average of the two determinations.
Column 11: Interstellar reddening, $E(B-V)$.
Column 12: Distance d, in kpc.
Column 13: Name of HII region found in the vicinity of the star. This does not necessarily mean that it is excited by this star.
Figure 5 gives the interstellar reddening $E(B-V)$, as a function of the distance. The general pattern is similar to that in plots published by Neckel & Klare (1980). We plotted with triangles the stars found on Schmidt plates in absorbed parts of the sky where the stellar density is faint and with circles those found in clear parts, where the stellar density is high. Filled symbols represent stars with accurate distances and open symbols represent rough distances determined from *UBV* photometry alone. Let us recall that these distances were determined assuming luminosity classes V, thus giving minima distances. Certainly some of the stars are giants or supergiants, so that the corresponding open symbols in Fig. 5 should be shifted toward larger distances. The absorption increases significantly between 1 and 2 kpc, when crossing the Sagittarius arm; this increase is higher for the stars found in absorbed parts of the sky, suggesting that the large absorbing cloud extended over several degrees in this part of the sky is located within the Sagittarius arm and not close to the Sun as is the case at $l = 300°$. Because of the low accuracy of the stellar distances there are no clearly separated patches on the plot, which would allow one to distinguish different spiral arms. The 17 O type stars of Table 3 are found at an average distance of 2.3 kpc, more or less indicative of the distance dominating the $l = 328°$area.
A few clusters are known in this region. Only Moffat 1 seems to be able to excite hydrogen. It contains a dozen early type stars associated with an M3Ia star. Moffat (1976) gives a distance of 2.1 kpc ± 0.2 kpc from *UBV* magnitudes for this cluster, in good agreement with our average value for O type stars.

5. Discussion

Before discussing the evaluation of the kinematic distances, we summarize in Table 4 the optical and radio velocities for HII regions and associated CO clouds in the observed area, around longitude 328°. The individual sources have been grouped in complexes on the basis of their position and velocity.
Column 1 gives the source identification: galactic coordinates for radio continuum sources, RCW number (Rodgers et al. 1960) or galactic coordinates (with prefix Hα) for HII regions detected at Hα wavelength only, galactic coordinates (with prefix CO) for molecular clouds we identified from CO maps by Bronfman et al. (1989).
Column 2 gives the dimension of the radiosource (Caswell & Haynes 1987) or the Hα dimension (given between parenthesis).
Column 3 gives the flux at 5 GHz (Caswell & Haynes 1987).
Column 4 gives the $V_{\rm LSR}$ of the source we derived from our Hα observations.
Columns 5 to 7 give the $V_{\rm LSR}$ found in the literature at radio wavelengths (with reference between parenthesis). We give respectively the velocity of the H109α recombination line, of the CO radio emission line, and of radio absorption lines H_2CO, OH and HI.
Column 8 gives the stellar distance from Table 3 as explained in Sect. 4. It is the adopted distance whenever available.
Column 9 gives the kinematic distance for each complex calculated as explained below in Sect. 5.1.3. We calculated this kinematic distance even for HII regions with a known stellar distance, but the latter was prefered everytime.

5.1. *Determination of kinematic distances*

5.1.1. Influence of the LSR values

To obtain kinematic distances we first of all correct the measured heliocentric radial velocities for the solar motion with respect to the Local Standard of Rest (LSR). The LSR is a fictitious point travelling at the mean velocity of the stars in the solar neighbourhood. The most often adopted solar motion is the "Standard Solar Motion" (u_0 = 10.4 km s^{-1}, v_0 = 14.8 km s^{-1}, w_0 = 7.3 km s^{-1}) which is determined with respect to stars forming the majority in the general catalogues of radial velocities and proper motions (Delhaye 1965, Mihalas & Binney 1981). It is this solar motion we have adopted for determining our $V_{\rm LSR}$ velocities in order to make comparison with other data easier.

One should remember however that the value of the solar motion depends on the stellar population (and on the distance of the sample) used to calculate it. For instance Delhaye (1965) determined the peculiar velocity of the Sun relative to the LSR with respect to a stellar population with negligible dispersion to be: $u_0 = 9$ km s^{-1}, v_0

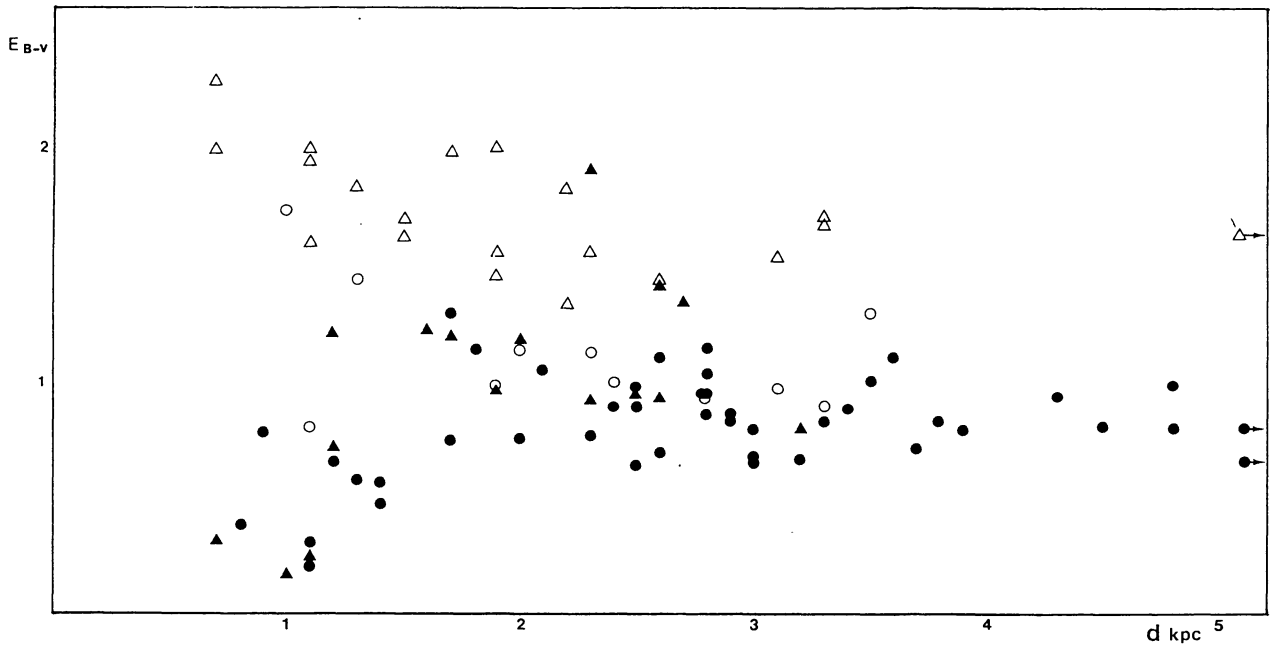

Fig. 5. Color excess of the OB3 stars as a function of the distance. Triangles are for stars situated in absorbed parts of the sky and circles for those situated in clear parts. Filled symbols correspond to stars with known spectral type and open symbols to stars with UBV alone (thus of smaller weight)

$= 12$ km s^{-1}, $w_0 = 7$ km s^{-1}. The kinematic determination of the solar motion with respect to OB stars (Balona & Feast 1974), HII regions (Crampton & Georgelin 1975) and Cepheids (Wilson et al. 1991) all lead to a value of u_0 around 7 km s^{-1} (note that this value of u_0 would not change very much if a different R_0 were used, see Georgelin 1975). Using this last value for u_0 instead of the above LSR value ($u_0 = 10.4$ km s^{-1}) leads to a correction of our derived $V_{\rm LSR}$ equal to $-3.4 \cos l$. Similarly, using CO velocities of molecular clouds and stellar distances of the associated HII regions, Brand (1986) and Fich et al. (1989) found a motion of the molecular gas with respect to the LSR (called V_m) around 4 km s^{-1} from $l = 180°$ to $l = 0°$ and corrected their $V_{\rm LSR}$ of $-V_{\rm m} \cos l$. Both corrections are about the same, suggesting that both molecular gas and HII regions have to be treated in the same manner.

The asymmetry between the northern and southern galactic rotation curves discussed by Kerr (1969) probably comes from the same phenomenon. Blitz & Spergel (1991) have argued that the observed outward motion of the LSR comes from a triaxial spheroid inside the solar circle. In their model the magnitude of this motion changes with R, the LSR receding from the galactic center at 14 km s^{-1} while the outermost HI gas is on nearly circular orbits.

At galactic longitude $l = 328°$ a correction of -3 km s^{-1} should be applied to the quoted $V_{\rm LSR}$ to take this effect into account.

5.1.2. Galactic rotation

In the following discussion we will use $\theta_0 = 220$ km s^{-1} and $R_0 = 8.5$ kpc as recommended by the IAU (Kerr & Lynden Bell 1986) although the present trend favours R_0 values between 7 and 8 kpc (Fich & Tremaine 1991, Feast 1987).

Most rotation curves of the Galaxy within the solar circle have been deduced from radio data. They are determined in each direction by the maximum velocity at the tangent point, that is to say by the velocity of only one region of the Galaxy at each longitude. Since they are average rotation curves they can be used for other regions only if the Galaxy obeys a pure circular rotation. As shown by irregularities seen on all rotation curves and on two dimensional velocity fields (e.g. Brand & Blitz 1993) this is obviously not the case in our Galaxy (moreover we have to realize that this is the rule for all galaxies). Systematic deviations from circular motions of about 10 km s^{-1} exist in many parts of the Galaxy. They are often due to peculiar motions related to spiral arms. As a consequence it is always better to use stellar distances when available because, even though they have their own (large) sources of error, they are independant of non circular motions.

5.1.3. Evaluation of the kinematic distances

At $l = 328°$ the maximum velocity is reached at 7.2 kpc from the Sun, so that radio rotation curves are not very useful at distances less than 7 kpc. In this direction devi-

ations of 10 km s^{-1} from the circular velocity may introduce errors of 0.5 kpc.

Despite the large uncertainties of stellar distances the best would be to use a relation between V_{LSR} and d_{kin} determined from both stellar distances and gas velocities in this part of the Galaxy. This is in fact the usual way of determining the velocity field and the rotation curve of the outer Galaxy (Jackson et al. 1979, Fich et al. 1989, Brand & Blitz 1993). For the inner Galaxy only Brand studied a part of the fourth quadrant, up to $l = 305°$, with CO velocities and distances of associated HII regions. Beyond, between $l = 305°$ and $l = 350°$, very few distances of exciting stars are known. We have determined the rotation velocity, θ, and the distance to the galactic center, R, for the few HII regions (given by Georgelin & Georgelin 1976) with known stellar distances in this sector of longitude at galactic radii between 6 and 8 kpc with the new values $R_0 = 8.5$ kpc and $\theta_0 = 220$ km s^{-1}. We find an average rotation velocity $\theta = 225 \pm 11$ km s^{-1} in good agreement with the values found by Brand & Blitz (1993) for the same R (see their Fig. 3) determined from HII/CO objects and HI terminal velocities.

However there is a discrepancy near longitude 328°, where θ values for the HII regions at d less than 2.5 kpc calculated from Tables 3 and 4 are systematically larger, by about 10 km s^{-1} ($\theta = 236 \pm 7$ km s^{-1}). Although this difference is marginally significant we conclude that the two groups of HII regions found with stellar distances 1 and 2.3 kpc at $l = 328°$ exhibit a deviation from pure circular motion. Such a deviation leads to reduce the distances of about 0.6 kpc with respect to kinematic distances obtained from the average rotation curve of Brand & Blitz 1993 (this reduction is 0.45 kpc when comparing with distances obtained using $\theta = 225$ km s^{-1}). The observed deviation was used to correct the kinematic distances of the HII regions with velocities ranging from -19 km s^{-1} to -42 km s^{-1} (Table 4). Let us note that this has little influence on our results since there are only 3 HII regions there with unknown stellar distance (which is the adopted distance whenever available).

There is no problem for the most negative velocities such as those found in the range -90 km s^{-1} to -100 km s^{-1} (see Table 3) corresponding to the tangent point around $d = 7.2$ kpc. However a serious problem is raised by intermediate velocities (-90 km s^{-1} < V_{LSR} < -40 km s^{-1}) because we are not sure whether a deviation from circular motion exists in the region of distance just above 2.5 kpc or not. The few stellar distances known around 3 kpc associated to the velocities of HII regions do not suggest such a deviation. For this velocity range we adopted an average rotation curve calculated by Brand & Blitz (1993) which is almost flat rotation curve. We also used this curve for objects with positive radial velocities (i.e. beyond the solar circle on the other side of the galactic center) but the most important error for such objects comes from the R_0 determination.

5.2. *Distances*

5.2.1. Spiral feature at -20 km s^{-1}

We have seen in Sect. 3 that there is a faint diffuse emission around -20 km s^{-1} all over the observed area. The contours of parts where this emission is enhanced are shown as dashed lines in Fig. 3b and the most interesting of them are mentioned in Table 3.

The CO maps published by Bronfman et al. (1989) show CO clouds probably associated with 3 of these HII regions. Furthermore 3 stars of Table 3 are good candidates for exciting 3 HII regions, namely: HD 142451, with spectral type B3V, at 1100 pc, close to the center of Hα 327.8 − 0.9; HD 141926, with spectral type B2IIIe, at 900 pc, probably associated with Hα 327.0 − 1.2 and HD 143752 with spectral type B3III, at 800 pc, probably associated with Hα 328.2 − 2.0. However these stars are of rather late type and one can ask whether they are capable of ionizing these HII regions or not. Typically a B3 type star ionizes a spherical HII region of 1.5 pc diameter (5 arcmin at 1 kpc) with density 2 cm^{-3} (Panagia 1973). Such an HII region would have an emission measure of 6 cm^{-6}, pc. Since we are probably not dealing with homogeneous spheres of hydrogen but with clumpy material, which tends to increase the observed emission measure, the intensity of the lines observed for both Hα 327.0 − 1.2 and Hα 328.2 − 2.0 seems to be fairly normal. In contrast Hα 327.8 − 0.9 appears too bright to be ionized by HD 142451 alone, but other stars not catalogued up to now could be responsible for the observed Hα brightness.

We conclude that the ionized gas we observe with a radial velocity around -20 km s^{-1} is at a distance of about 1 kpc. This gas marks the Sagittarius-Carina spiral arm at longitude 328° where it had not been detected up to now, neither optically nor at radio wavelengths.

5.2.2. Spiral features at -40 km s^{-1} and -50 km s^{-1}

As seen in Table 3 there is no HII region with velocity between -25 km s^{-1} and -37 km s^{-1}. This is probably due to a gap between two spiral arms and the HII regions with velocities between -40 km s^{-1} and -50 km s^{-1} certainly belong to the next spiral arm (Scutum-Crux). We have seen that the ionized hydrogen in the latter range of velocities appears as HII regions of much different shapes and brightnesses immersed in a faint diffuse emission detected all over the observed area. The diffuse emission is probably ionized by a large fraction of the OB stars of the area (listed in Table 3) with an average distance of 2.3 kpc. The Moffat 1 cluster, at 2.1 kpc, is in a rather faint intensity area and more or less located at the center of the ionized complex of roughly spherical shape (we will call it

the 328.5 − 1.0 region). This cluster certainly plays a role in the ionization of the diffuse emission.

Concerning the HII regions there are clearly two distinct groups, one with velocities near -40 km s^{-1} and another one with more negative velocities, down to -50 km s^{-1}. The first group contains the RCW 94-95 complex at 2.3 kpc and the associated radiosources near 326.5 + 0.7, it also contains the 328.5 − 1.0 region, the HII region RCW 98 and the other regions delineated with a continuous line in Fig. 3b.

We conclude that the average stellar distance of 2.3 kpc seems quite suitable for the whole ionized gas at -40 km s^{-1}.

The HII regions of the second group, with more negative velocities, are found only in the 328.5 − 1.0 region. The exciting stars of the brightest HII regions there (RCW96, RCW97 and RCW99) are not known. OB stars are indeed observed in the direction of RCW97 but none could be identified with certainty as being an exciting star. Furthermore their distance is poorly known since only UBV photometry is available for these stars. The few other exciting stars for other HII regions of the same group have distances around 3 kpc, suggesting that the second group is seen behind the first, along the same line of sight. This implies that the 328.5 − 1.0 region is not a single entity but is composed of at least two different layers seen along the same line of sight. The appearence of this extended complex in Fig. 1 suggests at first that it is a single entity since it looks like a large ring or bubble with minimum intensity at the center and filaments all around. Such a large bubble (120 pc in diameter) could however not have been formed in a galactic arm. Furthermore other arguments bring weight to the existence of two layers: First of all the HII regions observed from their recombination line at radio wavelengths all belong to the second velocity group, suggesting that this group contains HII regions intrinsically brighter. Furthermore both velocity values are often found together and there is no clear gradient from one value to the other one.

We conclude that there are two distinct groups of HII regions, one with velocities around -40 km s^{-1} at about 2.3 kpc and another one with velocities around -50 km s^{-1} at about 3 kpc, both belonging to the same spiral arm (Scutum Crux arm).

327.313 − 0.536 and RCW97: The radiosource 327.313 − 0.536 has been the most extensively studied of this area. Its center corresponds to a low intensity Hα emision as seen in Fig. 3a. The detection of infrared emission (Persson et al. 1976; Epchtein & Lepine 1981) and H_2O maser emission (Batchelor et al. 1980) suggest that there is a strong star formation activity there. RCW97, about 10 arcmin southwest of the radiosource, coincides with a minor peak of the radio continuum. The radial velocities of both objects are the same, indicating without no doubt that they belong to the same complex. The CO ($J = 2 \rightarrow 1$) emission has been mapped by Brand et al. (1984) in an area 14' × 14' around the radio peaks. They find a velocity gradient, with velocities going from -50 km s^{-1} in the NW to -46 km s^{-1} in the SE. At Hα wavelength we find an average velocity of -48 km s^{-1} for RCW97, in agreement with the CO velocities, but also a more negative component at -64 km s^{-1} in the northern part of RCW97, that is to say in the direction of the main radio peak. A CO component with the same velocity has been observed by Whiteoak et al. (1982). This component may be due to an ejection motion related to the active star formation quoted above just as the CO outflow found by Brand et al. 1984. It may be as well part of the radio complex at about -60 km s^{-1} to the west of the observed area. Despite the strong absorption in this direction we have seen that an Hα component is suspected there around -60 km s^{-1} (Sect. 3.2), furthermore the absorption is not so strong near RCW97.

Since an absorption line is observed at -37 km s^{-1} it is clear that the general diffuse Hα emission at -40 km s^{-1} is indeed in front of the RCW97 complex as we have concluded in the previous paragraph.

328.283 − 0.586: It is more difficult to know whether the radiosource 328.283 − 0.586 belongs to the same spiral arm, that is to say whether the near distance must be chosen when resolving the distance ambiguity. Whiteoak & Gardner (1974) mention a faint H_2CO line detected in absorption at -72 km s^{-1} for this radiosource. A similar line has been detected in the optically visible HII region RCW99 for which the near solution is clearly the right one. So the detection of an absorption line with a strongly negative velocity in 328.283 − 0.596 is certainly not a sufficient argument to assess that this source is very far away, especially when one takes into account its galactic latitude.

This radiosource is close to Hα condensations although it coincides with none of them. We decided to include it in the group related to Hα 328.4 − 0.5 since it has the same velocity.

An H_2CO absorption line at -78 km s^{-1} has also been found in the radiosource 327.985 − 0.086, the velocity of which is -45 km s^{-1}. It is not clear whether it is the same phenemenon or whether this source is indeed at the far distance.

5.2.3. Spiral feature at -72 km s^{-1}

Two seemingly linked radiosources 327.612 − 0.354 and 327.759 − 0.351 are part of this complex. In the CO maps by Bronfman et al. (1989) we have found a CO cloud with similar velocity; centered on 327.75 − 0.4 it extends up to $l = 328.5$. This is probably the cloud responsible for

the absorption line at -72 km s^{-1} observed in 328.283 − 0.586 as well as RCW99.

As seen in Sect. 3.4 at Hα wavelength we detected ionized gas at about -65 km s^{-1} at the position of the second source (327.759 − 0.351). We conclude that this radiosource being detected in Hα is at the near distance. Assuming that this part of the Galaxy has no strong deviation from the circular rotation the velocity indicates a distance of 4.5 kpc. Although it is not very far this is the most distant HII region detected at Hα wavelength in this area.

This difficulty in trying to detect far away HII regions may be logically explained by the rather strong absorption observed at this galactic longitude since we observe at only 30° from the galactic center, but also by the relatively small number of radiosources there, statistically diminishing the chances of positive detection at optical wavelengths.

5.2.4. Feature at -60 km s^{-1}

Several radiosources (HII regions as well as molecular clouds) have velocities between -53 km s^{-1} and -64 km s^{-1}. Their shape is not clearly defined as seen on maps by Caswell & Haynes (1978) in radiocontinuum at 5 GHz. It is not clear whether it is a single complex or several separate regions. Their wide extension as well as the lack of an H_2CO component with more negative velocity strongly suggest that its distance is the one indicated by the near solution. We have seen in Sect. 3.2 that a very faint Hα emission is suspected at the position of these radiosources.

5.2.5. Feature at -90, -100 km s^{-1}

Three complexes are found at these velocities at 324.1 + 0.2, 328.3 + 0.4 and 329.5 + 0.2, all lying probably near the tangent point of the Norma spiral arm at about d = 7 kpc (assuming $R_0 = 8.5$ kpc). As could be expected, no Hα has been detected in this direction.

6. Conclusions

The detailed velocity field of the ionized hydrogen (diffuse emission and HII regions) over an area of 4° × 3° centered at galactic longitude 328° has been obtained for the first time. Previous observations (optical and radio) only covered the brightest HII regions of this area.

Our Hα observations together with stellar and radio data lead to the following conclusions:

- A faint nebular emission exists all over the observed area, without any actual void.
- There are always several ionized gas layers along the line of sight. Two velocity groups are seen almost everywhere, one around $V_{LSR} = -20$ km s^{-1} and another one around $V_{LSR} = -40$ to -50 km s^{-1}.
- The ionized gas layer observed around -20 km s^{-1} is at about 1 kpc from the sun. It is most probably part of the Sagittarius-Carina spiral arm observed at a longitude where it had not been observed up to now. This relatively homogeneous gas layer is seen in front of the main HII regions seen in this area, most of them belonging to the Scutum-Crux arm.
- This second spiral arm appears in fact at this longitude as composed of 2 distinct gas layers along the line of sight, one with velocity -40 km s^{-1} at 2.3 kpc and another one with velocity -50 km s^{-1} at about 3 kpc. Absorbing clouds (probably inside the arm) add complexity to the situation, for instance optically visible HII regions barely coincide with the maximum of the radioemission (e.g. RCW97 and 328.283 − 0.596) and the detection of radiosources at Hα wavelength is not at all systematic.
- A radio complex located still further behind these regions, at about 4.5 kpc, has also been detected at Hα wavelength in our Survey. This is quite remarkable in the sense that this ionized gas is detected behind 3 other layers of ionized gas.

In the adjacent galactic areas more distant HII regions will be searched for, but, being closer to the inner absorbed part of the Galaxy, they could be still more difficult to detect.

Acknowledgements. We thank Prof. L. Woltjer who initiated this Survey in La Silla and ESO for providing lodging of the observers, we also thank INSU for financial support of this Survey. We are indebted to A. Viale for her help with the data reduction and to S. Arzano for preparing this article in LaTeX. This research has made use of the Simbad database, operated at CDS, Strasbourg, France.

References

Amram P., Boulesteix J., Georgelin Y.M. et al. 1991, The Messenger 64, 44
Balona L.A., Feast M.W. 1974, MNRAS 167, 621
Bassino L.P. 1985, AJ 90, 2249
Bassino L.P., Dessaunet V.H., Muzzio J.C., Waldhausen S. 1982, MNRAS 201, 885
Batchelor R.A., Caswell J.L., Goss W.M. et al. 1980, Austral. J. Phys. 33, 139
Blitz L., Spergel D.N. 1991, ApJ 370, 205
Bok B.J., Bok P.F., Graham J.A. 1963, PASP 75, 514
Bok B.J., Gollnow H., Mowat M. 1967, The Observatory 87, 250
Brand J. 1986, Ph. D. Thesis, University of Leiden
Brand J., Blitz L 1993, A&A 275, 67
Brand J., Van der Bij M.D.P., de Vries C.P. et al. 1984, A&A 139, 181
Bronfman L., Alvarez H., Cohen R.S., Thaddeus P. 1989, ApJS 71, 481
Caswell J.L., Haynes R.F. 1987, A&A 171, 261

Cohen R.S., Grabelsky D.A., Alvarez H. et al. 1985, ApJ 290, L15
Crampton D., Georgelin Y.M. 1975, A&A 40, 317
Delhaye J. 1965, "Solar Motion and Velocity Distribution of Common Stars", Galactic Structure (Blaauw & Schmidt, Chicago) 61
Drilling J.S. 1972, AJ 77, 463
Drilling J.S. 1991, ApJS 76, 1033
Drilling J.S., Perry C.L. 1981, A&AS 45, 439
Epchtein N., Lepine J.R.D. 1981, A&A 99, 210
Feast M.W. 1987, "Galactic distances scales", The Galaxy (Gilmore & Carswell, Reidel) 1
Fich M., Blitz L., Stark A.A. 1989, ApJ 342, 272
Fich M., Tremaine S. 1991, "The mass of the Galaxy" ARA&A 29, 409
Gardner F.F., Whiteoak J.B. 1984, MNRAS 210, 23
Garrison R.F., Hiltner W.A., Schild R.E. 1977, ApJS 35, 111
Georgelin Y.M. 1975, Thesis, Université de Provence
Georgelin Y.P., Georgelin Y.M. 1970a, A&A 6, 349
Georgelin Y.P., Georgelin Y.M. 1970b, A&AS 3, 1
Georgelin Y.M., Georgelin Y.P. 1976, A&A 49, 57
Gillespie A.R., Huggins P.J., Sollner T.C.L.G. et al. 1977, A&A 60, 221
Goss W.M., Manchester R.N., Robinson B.J. 1970, Aust. J. Phys. 23, 559
Goss W.M., Radhakrishnan V., Brooks J.W., Murray J.D. 1972, ApJS 24, 123
Haynes R.F., Caswell J.L., Simons L.W.J. 1978, Aust. J. Phys. Astrophys. Suppl. 45, 1
Humphreys R.M. 1975, A&AS 19, 243
Humphreys R.M., McElroy D.B. 1984, ApJ 284, 565
Jackson P.D., Fitzgerald M.P., Moffat A.F.J. 1979, Recent evidence on the rotation curve of our Galaxy for $R > R_0$, IAU Symp. 84, 221
Klare G., Neckel Th. 1977, A&AS 27, 215
Kerr F.J. 1969, ARA&A 7, 39
Kerr F.J., Lynden Bell D. 1986, MNRAS 221, 1023
le Coarer E., Amram P., Boulesteix J. et al. 1992, A&A 257, 389 (Paper I)
le Coarer E., Rosado M., Georgelin Y.P. et al. 1993, A&A 280, 365
Lynga G. 1964, Medd. Lunds Astron. Obs. Serie II, 140
Marcelin M., Amram P., Boulesteix J. et al. 1994, Hα survey of the Milky Way and Magellanics Clouds, IAU Symp. 161
Mc Gee R.X., Newton L.M. 1981, MNRAS 196, 889
Mihalas D., Binney J. 1981, Galactic Astronomy (San Francisco, Freeman) 398
Moffat A.F.J. 1976, A&A 50, 429
Muzzio J.C., Forte J.C. 1975, AJ 80, 1037
Neckel T., Klare G. 1980, A&AS 42, 251
Panagia N. 1973, AJ 78, 929
Persson S.E., Frogel J.A., Aaronson M. 1976, ApJ 208, 753
Robinson B.J., Caswell J.L., Goss W.M. 1971, Astrophys. Letters 9, 5
Rodgers A.N., Campbell C.J., Whiteoak J.B. 1960, MNRAS 121, 103
Rydgren A.E. 1974, PASP 86, 363
Shaver P.A., McGee R.X., Pottasch S.R. 1979, Nature 280, 476
Shaver P.A., McGee R.X., Newton L.M. et al. 1983, MNRAS 204, 53
Schild R.E., Garrison R.F., Hiltner W.A. 1983, ApJS 51, 321
Schmidt Kaler Th., 1983, Landolt-Borstein, New Series, Group VI Vol. 2B (Springer) 14
Stephenson C.B., Sanduleak N. 1971, Publ. Warner and Swasey Obs. 1, 100
Westerlund B.E. 1969, AJ 74, 882
White G.J., Phillips J.P. 1982, "CO $J = 2$-1 observations of southern galactic plane HII regions", Regions of recent star formation (Roger & Dewdney) 231
Whiteoak J.B., Otrupcek R.E., Rennie C.J. 1982, Proc. ASA 4, 434
Whiteoak J.B., Gardner F.F. 1974, A&A 37, 389
Wilson T.L., Mezger P.G., Gardner F.F., Milne D.K. 1970, A&A 6, 364
Wilson T.D., Barnes T.G., Hawley S.L., Jefferys W.H. 1991, ApJ 378, 708

Table 3. Distances of OB stars in the $l = 328°$ area

(1) No LSS	(2)	(3) SP	(4) (SP)	(5) V	(6) B-V	(7) U-B	(8) β	(9) V_{hel} (km/s)	(10) M_v	(11) E	(12) d kpc	(13)
3386		O6f		10.95	1.61	0.44		-30	-6.8	1.92	2.3	RCW94
	BDMW123		(07V)	12.87	1.38	0.20			(-5.0)	(1.70)	(3.3)	RCW95
	BDMW126		(B0.5V)	13.09	1.28	0.24			(-3.6)	(1.56)	(2.3)	
	BDMW128		(O9V)	11.58	1.39	0.24			(-4.5)	(1.70)	(1.5)	327.013+0.387
3401	-53°6701	B1II		10.41	0.70	-0.32	2.609	-31	-4.6	0.95	2.5	
3402	140926	B2IVne		7.91	-0.02	-0.75			-3.1	0.25	1.1	
3404	-53°6706	B1IV		10.86	0.66	-0.24		-31	-3.8	0.92	2.3	
	BDMW131		(O9.5V)	11.69	1.15	0.06			(-4.2)	(1.46)	(1.9)	
3405	-54°6706	B1III		10.63	0.67	-0.28	2.609	-5.3	-4.2	0.93	2.6	
	141318	B1III		5.72	0.06	-0.71	2.600		-4.4	0.32	0.7	
	MFIII13		(B2V)	13.83	1.76	0.78			(-2.5)	(2.00)	(1.1)	RCW97
	MFIII14		(O6.5V)	12.47	1.68	0.48			(5.1)	(2.00)	(1.9)	RCW97
	MFIII12	B0.5V		11.80	0.91	0.06	2.654	-28	-3.1	1.19	1.7	RCW97
3410			(B2V)	11.73	0.97	0.12			(-2.5)	(1.21)	(1.2)	
	MFIII15		(B3V)	14.67	1.64	0.77			(-1.6)	(1.84)	(1.3)	RCW97
	MFIII7		(O5V)	13.58	1.30	0.12			(-5.4)	(1.63)	(6.1)	
	MFIII17		(B1.5V)	14.48	1.73	0.74			(-2.8)	(1.98)	(1.7)	RCW97
	MFIII6		(B1.5V)	15.00	1.42	0.46			(-2.8)	(1.67)	(3.3)	
	MFIII18		(B2V)	12.30	0.75	-0.05			(-2.2)	(0.99)	(1.9)	RCW97
	MFIII19		(B1.5V)	13.38	1.70	0.71			(-2.8)	(1.95)	(1.1)	
	-52°9018		(B2V)	10.29	0.47	-0.33	2.656		2.4	0.71	1.2	
	BDMW134		(O9.5V)	11.02	1.68	0.51			(-4.2)	(1.99)	(0.7)	
	MFIII2		(B1.5V)	14.59	1.58	0.61			(-2.8)	(1.83)	(2.2)	
	141782	B1-2Vn		8.73	0.00	-0.43	2.698		-1.7	0.17	1.0	
	MFIII9		(O9V)	11.99	1.98	0.79			(-4.5)	(2.29)	(0.7)	
3416	-55°6764		(B0.5V)	11.56	0.66	-0.31			(-3.6)	(0.94)	(2.8)	
3417	141926	B2:III:e		8.60	0.55	-0.43			-3.7	0.79	0.9	Hα327.0-1.2
3420	-53°6768	B1Ib		9.18	0.60	-0.35		-26	-5.8	0.80	3.2	
	MFIII11		(B1.5V)	13.75	1.20	0.26			(-2.8)	(1.45)	(2.6)	
3421	142152	B0.5III		9.63	0.37	-0.55	2.590	-47	-4.8	0.65	3.0	
3422	-55°6802		(B2IV)	10.88	0.52	-0.28	2.634		3.0	0.76	2.0	
	MFI117		(B2V)	12.90	0.66	-0.16			(-2.5)	(0.90)	(3.3)	RCW98
	MFI118	B1Vn		12.38	0.86	-0.28	2.597		-3.9	1.12	3.6	RCW98
3423	-54°6791	O9.5IV		10.40	0.56	-0.47	2.610	-45	-4.5	0.86	2.8	RCW98
	MFI119		(B0V)	12.97:	1.31	0.23			(-3.8)	(1.61)	(2.3)	
	142237	B2IVne		8.80	0.11	-0.50			-2.4	0.31	1.1	
	MFI38	B1IV+B?		12.18	1.03	-0.02	2.564		-3.8	1.29	(3.5)	double star
	MFI87		(B2.5V)	12.87	0.79	0.00			(-2.0)	(1.04)	(2.1)	
3424	-54°6807	BOIII		9.96	0.42	-0.51	(2.618)	-35	-4.3	0.70	2.6	
	MFI10	B2V		11.32	0.51	-0.20	2.664	-2	-2.1	0.75	1.7	

Table 3. continued

(1) No LSS	(2)	(3) SP	(4) (SP)	(5) V	(6) B-V	(7) U-B	(8) β	(9) V_{hel} (km/s)	(10) M_v	(11) E	(12) d kpc	(13)
3425	-54°6818		(O6V)	10.42	0.71	-0.35	2.580		-5.0	1.04	2.8	
3426	-54°6818	B1Ib		10.51	1.21	0.11	2.556	-43	-6.3	1.42	3.0	Hα328.0-0.5
	MFI15	B0.5Iab		10.70	0.59	0.44	2.552	-48	-6.0	0.80	7.0	Hα328.0-0.5
	BDMW143		(O9.5V)	11.70	1.32	0.19			(-4.2)	(1.63)	(1.5)	
	142451	B3V		9.23:	0.02	-0.54	2.697		-1.6	0.22	1.1	Hα327.8-0.9
3429	142468	B0.8Ia		7.90	0.59	-0.41	2.549	-48	-7.0	0.80	3.0	Hα327.9-0.8
3430	-53°6850	B1V		10.99	0.50	-0.37	2.615	-41	-3.3	0.76	2.3	Hα328.2-0.5
	MFI90		(B2.5V)	12.71	0.67	-0.13	2.669		-2.0	0.89	2.5	
3431	-55°6837		(B0.5V)	10.67	0.36	-0.52	2.630		-3.3	0.64	2.5	
3432	-54°6846	B0.5III		10.35	0.43	-0.52	2.600	-38	-4.7	0.72	3.7	
	BDMW146		(B0.5V)	11.69	1.46	0.37			(3.6)	(1.74)	(1.0)	
3433	142565	B0.5Ib		8.99	0.46	-0.48	2.583	-37	-5.5	0.68	3.0	Hα327.9-0.8
3434	53°6867		(B0.5V)	11.05	0.77	-0.21	2.610		-3.8	1.05	2.1	Hα328.4-0.5
	MFI43		(B2.5V)	14.27	1.31	0.43			(2.0)	(1.56)	(1.9)	
	MFI96		(B1V)	12.28	0.57	-0.31			(-3.2)	(0.83)	(3.8)	
3435	142634		(O9.5IV)	8.70	0.67	-0.38	2.586		-4.9	0.97	1.9	double star
3436	-54°6858		(B2.5IbII)	10.71	0.60	-0.28	2.580		-5.0	0.81	4.8	
3437	-53°6872	B1V		11.89	0.56	-0.36	2.606	-59	-3.9	0.82	4.5	Hα328.4-0.5
	-54°6867		(B3V)	10.87	0.46	-0.21	2.671		-1.6	0.66	1.2	
3440	142775	B0Iab		9.13	0.71	-0.32	2.575	-31	-6.0	0.94	2.8	
	MFI48		(B2.5V)	13.31	0.88	0.08			(-2.0)	(1.13)	(2.3)	
	MFI47		(B2.5V)	13.88	1.08	0.24			(-2.0)	(1.33)	(2.2)	
	MFI33		(B2V)	14.74	1.30	0.39			(-2.5)	(1.54)	(3.1)	
	MFI50		(B3V)	13.38	0.80	0.08			(-1.6)	(1.00)	(2.4)	
	D14			11.87	0.88	-0.06			(-3.2)	(1.14)	(2.0)	
	MFI16	O8V		11.57	1.06	-0.09	2.586	-32	-4.8	1.37	2.7	
	MFI124		(B2V)	12.58	1.21	0.32			(-2.5)	(1.45)	(1.3)	
	MFI109		(B2V)	12.93	0.73	-0.07			(-2.5)	(0.97)	(3.1)	
	MFI108		(B3III)	12.44	0.85	0.08	2.625		-3.1	1.11	2.6	
3443	-54°6898	O7III		10.96	1.10	0.04	2.562	(-41)	-5.5	1.42	2.6	
3444	-53°6923		(B0.5III)	9.85	0.95	-0.09	2.58		-5.0	1.23	1.6	
	MFI35		(B3V)	13.58	1.40	0.55			(-1.6)	(1.60)	(1.1)	
3445	-53°6932		(O7V)	10.30	0.86	-0.23	2.59		-4.9	1.18	2.0	Cl Moffat 1
3447	-53°6950	O9.5II		9.75	0.53	-0.50	2.580		-5.4	0.83	3.3	Cl Moffat 1
3448	-53°6954		(B0.5V)	11.20	0.62	-0.33	2.62		-3.5	0.90	2.4	Cl Moffat 1
3449	-54°6948	B2:III:nne		11.312	0.63	-0.43		-37	-3.7	0.87	2.9	
	143218	B3III		9.60	0.37	-0.35	2.64		-2.9	0.57	1.4	
3450	-53°6964		(B1V)	11.71	0.41	-0.47	2.65		-2.9	0.67	3.2	

Table 3. continued

(1) No LSS	(2)	(3) SP	(4) (SP)	(5) V	(6) B-V	(7) U-B	(8) β	(9) V_{hel} (km/s)	(10) M_v	(11) E	(12) d kpc	(13)
3451	-53°6980		(B0III)	10.81	0.86	-0.19	2.58		-5.0	1.15	2.8	Cl Moffat 1
	D25		(B2II)	11.32	0.73	-0.19	2.59		-4.8	0.95	4.3	
3453	-53°6992		(B2V)	10.27	0.56	-0.22	(2.73)		(-2.5)	(0.80)	(1.1)	
3455	-55°7003	B0Ib		10.49	0.76	-0.29	(2.58)	-44	-6.0	1.00	4.8	
3457	-54°6990		(B0V)	11.33	0.59	-0.40	2.60		-4.1	0.89	3.4	
3458	-54°6991		(B3II)	11.54	0.46	-0.35	2.59		-4.7	0.65	7.0	
	143752	B3III		8.37	0.19	-0.34	2.68		-2.4	0.39	0.8	Hα328.2-2.0
3459	-54°6995		(B0IV)	10.82	0.65	-0.36	2.60		-4.4	0.95	2.8	
	-53°7041		(B2.5V)	10.38	0.36	-0.35	2.67		-2.0	0.58	1.3	
3461	-59°9235		(B0.5IV)	10.90	0.51	-0.42	2.60		-4.5	0.79	3.9	
3462	-53°7073	O9III		10.52	0.99	-0.11	2.61	-23	-4.6	1.30	1.7	
3463	-53°7082		(B0III)	9.80	0.84	-0.19	2.585		-5.0	1.14	1.8	
3466	-53°7090	B0.5Iab		9.34	0.80	-0.26	2.574		-6.5	1.01	3.5	
3468	-53°7124		(B1III)	10.52	0.58	-0.33	2.60		-4.4	0.84	2.9	
	144320	B2IVep		9.19	0.24	-0.55			-3.1	0.48	1.4	

Table 4. HII region complexes in the $l = 328°$ area

(1) Object	(2) d ('arc)	(3) S (Jy)	(4) Hα (km/s)	(5) H109α (km/s)	(6) V_{LSR} CO (km/s)	(7) abs (km/s)	(8) d⋆ kpc	(9) d_{kin} kpc
324.147+0.231	3.5	4.4		-91 (1)				
324.192+0.109	1	3.4		-92 (1)	-89 (3)	-93,-50,-30 (5)		6.9
				-87 (2)	-89,-79,-56,-29 (4)	-90,-69,-50,-29 (1)		
324.954+0.584	6.1	3.3		25 (1)				16.8
CO 325.3-0.1					28 (6)			
RCW94=326.315+0.689	30	30	-44	-45 (1)				
RCW94-1=326.24+0.69			-43	-43 (7)				
RCW94-2=326.41+0.78			-40	-40,-52 (7)				
RCW94-3=326.31+0.74			-44	-45 (7)				
RCW94-4=326.18+0.96			-40	-40 (7)				
326.230+0.976			-42	-42 (1)				
326.441+0.914	0.9	6.8	-40	-39 (1) (2) (7)	-86,-41 (4)	-40 (5)	2.3	2.3
326.645+0.589	(15)	34.9	-43	-44 (1) (7)	-41 (3)	-43,-22 (5)		
				-45 (2)	-100,-84,-41,-22 (4)	-44,-21 (10)		
					-39 (8)	-45,-21 (11)		
CO 326.6+0.6					-41 (9)			
RCW95=326.716+0.783	(3)		-43					
327.013+0.387	(15)		-43					
326.141-0.328	12	16.4		-65 (1)				
326.441-0.396	12	18.0		-61 (1)				
326.660-0.471	9	11.2		-57 (1)				
326.718-0.564	12	18		-56 (1)				
CO 326.8-0.6					-60 (9)			3.8 or 10.5
326.959+0.031	9	19.6		-64 (1)		-57,-46 (5)		
326.985-0.158	12	27.3		-53 (1)		-61,-45,-38 (1)		
327.023-0.315	4.2	4.7		-61 (1)		-61(1)		
Hα 327.0-1.2	(5)		-23					
CO 326.2-0.9					-19 (9)		0.9	1.0
RCW96(326.9-1.0)	(2)		-50					3.1
RCW97(327.2-0.5)	(10)		-48,(-64)	-49 (7)				
327.313-0.536	0.9	32.6		-48 (1)	-47 (3)	-49,-37 (1,5)		
				-49 (2)	-64,-47,-37 (4)	-49 (11)		
				-47 (8)	-47 (8)	-50,-38,-14,-4,2 (14)		3.1
				-49 (12)	-47 (13)			
				-51,-39 (12)				
CO 327.25-0.6					-47 (9)			
CO 327.2-0.3					-60 (9)			3.9 or 10.5
RCW98=327.5-0.8	(8)		-37		-37 (9)		2.8	2.1
327.612-0.354	4.2	5.8		-72 (1)		-70 (5)		
				-70 (2)		-74 (1)		
327.759-0.351	4.2	5.7	-65	-72 (1)		-76 (5)		4.5
						-75 (1)		
CO 327.75-0.4					-75.9 (9)			
Hα 327.8-0.9	(6)		-19				1.1	0.9
CO 328.4-0.7					-18 (9)			
327.834+0.113	11	14.3		-100 (1)	-93 (9)			7.2

Table 4. continued

(1) Object	(2) d ('arc)	(3) S (Jy)	(4) Hα (km/s)	(5) H109α (km/s)	(6) V_{LSR} CO (km/s)	(7) abs (km/s)	(8) d⋆ kpc	(9) d_{kin} kpc
Hα 327.9-0.8	(15)		-46					
CO 327.9-0.6					-46 (9)		3.0	3.1
Hα 328.0-0.5	(6)		-43					
Hα 328.2-0.5	(1)		-47					
327.985-0.086	3.5	4.9		-45 (1) (2)		-78,-44 (5)		3.0 or 11.4
CO 327.9+0.0					-43 (9)			
Hα 328.2-2.0	(5)		-25				0.8	1.3
328.283-0.586	4.9	3.6		-43 (1) (2)	-70,-43,(-19) (4)	(-72),-43 (5)		
						-42 (1)	(3.3)	3.0
Hα 328.4-0.5	(7)		-43					
328.310+0.448	2.6	8.3		-97 (1)		-96 (5)		
				-96 (2)		-92,-52 (1)		6.0
SNR 328.4+0.2						-90,-69,-44 (5)		
CO 328.3+0.4					-95 (9)			
CO 328.5-0.1					30 (6)			(18)
RCW99=328.593-0.518	3.5	11.9	-52	-51 (1)	-71,-48 (4)	(-72),-46 (5)		3.2
					-48 (9)			
328.806-0.083	4	2.5		-47 (1)		-35,-78 (1)		3.2 or 11.3
328.812+0.637	2.6	1.8		-42 (1)	-40 (9)	-100,-39 (1)		2.3 or 11.7
CO 328.85-0.15					-21 (9)			
Hα 328.7-0.3	(10)		-22					1.1
329.353+0.144	3.5	4.6		-107 (1)		-106,-85 (1)		
329.489+0.207	5	3.9		-102 (1)		-100 (1)		7.3
CO 329.6+0.3					-102 (9)			
330.041-0.045	2.6	1.3		-38 (1)		-45 (1)		2.6 or 12.0
330.305-0.385	3.5	1.7		-76 (1)		-80 (1)		5.9

References:
(1) Caswell & Haynes (1987), (2) Wilson et al. (1970), (3) Gillepsie et al. (1977), (4) Whiteoak et al. (1982), (5) Whiteoak & Gardner (1974) and Gardner & Whiteoak (1984), (6) Cohen et al. (1985), (7) Shaver et al. (1983), (8) White & Philips (1982), (9) estimated from Bronfman et al. (1989), (10) Goss et al. (1970), (11) Robinson et al. (1971), (12) McGee & Newton (1981), (13) Brand et al. (1984), (14) Goss et al. (1972),

Notes:
Hα327.0 - 1.2 $\alpha = 15^h50^m7$ δ = -55°12'
Hα327.8 - 0.9 $\alpha = 15^h53^m2$ δ = -54°23'
Hα327.9 - 0.8 $\alpha = 15^h53^m4$ δ = -54°12'
Hα328.0 - 0.5 $\alpha = 15^h52^m9$ δ = -53°56'
Hα328.2 - 0.5 $\alpha = 15^h53^m5$ δ = -53°49'
Hα328.2 - 2.0 $\alpha = 16^h\ 0^m8$ δ = -54°58'
Hα328.4 - 0.5 $\alpha = 15^h54^m3$ δ = -53°45'
Hα328.7 - 0.3 $\alpha = 15^h55^m6$ δ = -53°22'